Current Research in Food Science 12 (2026) 101392

Contents lists available at ScienceDirect

Current Research in Food Science

journal homepage: www.sciencedirect.com/journal/current-research-in-food-science

Konjac glucomannan-based nano-fiber membrane delivery system for enhancing anthocyanins stability and regulating oral mucosalpermeation

Falin Sun [a,1], Guoqiang Zhang [b,1], Qingying Dong [b], Baoru Yang [c], Ying Zhou [c], Rodrigo Quintana Loyola [d], Yanzhe Alfonso Ren [e], Bin Li [a], Jinlong Tian [a,*]

[a] College of Food Science, Shenyang Agricultural University, Shenyang, Liaoning, China
[b] Wuhu Green Food Industrial Research Institute Co., Ltd., Wuhu, 241000, China
[c] Food Sciences, Department of Life Technologies, University of Turku, Turku, Finland
[d] Agricultural Research Institute INIA Chile, Chile
[e] Importadora exportadora Mateo spa, Chile

ARTICLE INFO

Handling Editor: Dr. Xing Chen

Keywords:
Electrospinning
Anthocyanin
Nano-fiber membrane
Oral absorption
Sustained release

ABSTRACT

This study develops a core-shell hydrogel nanofiber membrane (NFM) via dynamic rheology-guided spinning and multi-component molecular design to enhance stability and bioactive delivery efficiency. The Konjac glucomannan (KGM)/Polyvinylpyrrolidone (PVP) core forms a 3D gel barrier through hydrogen bonds, inhibiting anthocyanin diffusion (PVP/KGM/ACNs@PVA 6.48 MPa mechanical strength) and enabling 97% release in 120 min. The Polyvinyl alcohol (PVA) shell stabilizes the interface via dynamic hydrogen bonds, achieving 81.22% retention after 8-day light exposure. Cytotoxicity assessment confirmed its good biocompatibility. In addition, NFM can achieve controlled release with a release rate of 97% within 120 min and has a high penetration rate in pig mucosa, with a penetration rate of 53.96% within 5 h. After penetration, it still retains significant antioxidant activity, verifying the feasibility of oral absorption. These findings highlight a rheology-driven strategy for efficient bioactive component delivery.

1. Introduction

Anthocyanins (ACNs) are a class of water-soluble phenolic pigments that are formed by the glycosidic linkage of anthocyanidins (the aglycones) with one or more sugar moieties. Research has demonstrated that these compounds possess significant antioxidant properties, the ability to regulate lipid metabolism, and the potential to enhance immune function (Song et al., 2023). However, the absorption rate of anthocyanin is poor in practical applications (Choudhary and Lizarazo). Especially in the alkaline environment of the small intestine and metabolic catabolism of the intestinal flora limits the bioavailability (Tang et al., 2024). Therefore, it is of great research value to develop novel transmembrane absorption pathways of ACNs via the oral mucosa in response to the need for optimization of active ingredient bioavailability (Pandey et al., 2022). This delivery method can be absorbed directly through the mucosal capillaries, effectively avoiding the first-pass metabolism effect in the gastrointestinal tract, especially for the active compounds that are unstable and easy to be degraded in the intestinal environment is a good choice (Kali et al., 2023).

As an innovative delivery system, the nano-fiber membrane (NFM) can be absorbed directly into the blood circulation through the oral mucosa, effectively circumventing the first-pass metabolism effect in the gastrointestinal tract and improving the bioavailability of the active ingredients (Serrano et al., 2019). NFM has the physical properties of lightness and flexibility with the advantage of convenient carrying, and it has realized large-scale application in the field of drug delivery, but there is still a large research space in the field of functional food development. It is especially worthwhile to pay attention to the fact that the research on the absorption of natural active ingredients represented by ACNs in membrane formulations is still at the forefront. By constructing an ACNs delivery system based on oral membrane technology, we can not only break through the technical bottlenecks of traditional dosage forms in terms of stability, absorption efficiency and applicability to the population, but also provide innovative solutions for the development of universal nutritional fortification products.

Various methods have been proposed to produce NFM, of which

* Corresponding author. Dongling Road, Shen he District, Shenyang, Liaoning, 110866, China.
E-mail address: sweet_vs_sweet@163.com (J. Tian).
[1] These authors contributed equally to this work and should be considered as co-first authors.

https://doi.org/10.1016/j.crfs.2026.101392
Received 27 November 2025; Received in revised form 25 February 2026; Accepted 23 March 2026
Available online 27 March 2026

electrostatic spinning is a simple, straightforward, low-cost and versatile technique. The principle is to use a high-voltage electric field to drive a polymer solution or melt to form a Taylor cone and achieve jet stretching to prepare nanofiber materials with unique physicochemical properties (Sun et al., 2025). Coaxial electrostatic spinning creates core-shell structures through precisely controlled coaxial jetting of core and shell fluids (Zhao et al., 2024). However, most of the coaxial nanofibers need to be formed by some physical and chemical means such as photo-crosslinking, electron beam-assisted crosslinking, chemical crosslinking, and enzyme-activated crosslinking, which are complicated and inedible (Zhao et al., 2024). To address this issue, this study proposes an innovative strategy based on physical interactions: forming a "spatial interlocking structure" through mutual penetration between the core layer and shell layer to construct edible core-shell structured nanofiber membranes. This method eliminates chemical cross-linking steps, simplifies the preparation process, and ensures the edible safety of the final product, providing a more viable carrier system for applications in the functional food sector.

In recent years, natural plant polysaccharides have been widely used in food engineering (Su et al., 2024). Konjac glucomannan (KGM) is a natural plant polysaccharide extracted from konjac tubers. Its main chain consists of D-glucose and D-mannose connected by β-1,4 glycosidic bond. Through molecular chain entanglement and intermolecular interactions between high molecular weight KGM and PVP, a network-like structure capable of significantly enhancing viscosity was constructed within the spinning solution. The core solution is crucial for suppressing the migration of ACNs during electrospinning and maintaining the unique core-shell interface (Li et al., 2021). Polyvinylpyrrolidone (PVP) was introduced as a spinning aid and carrier polymer, primarily to regulate solution viscosity and provide sufficient polymer chain entanglement. These properties are beneficial for stabilizing the coaxial electrospinning jet and are therefore conducive to the formation of continuous coaxial fibers (Kurakula and Koteswara Rao, 2020). Polyvinyl alcohol (PVA) has excellent structural stability and processability. The remarkable viscoelastic properties of its solution enable it to form a continuous and uniform shell layer structure in the electrostatic spinning process, thus realizing the effective encapsulation of the core material. It prevents the degradation of the core material and realizes the continuous release of the core layer, thus acting as a shell layer.

To avoid degradation of ACNs by intestinal flora and alkaline pH in the gastrointestinal tract. We hypothesized a paradigm shift from traditional oral administration to transmucosal absorption via the oral cavity, taking advantage of the rich vascular network of the oral mucosa. Enhanced stability and absorption efficiency of ACN. NFM loaded with ACNs were prepared by coaxial electrostatic spinning to improve the bioavailability of ACNs. With PVA as the shell layer and PVP/KGM/ACNs as the core layer, the core-shell structure is constructed by interpenetrating the core-shell layers to form a "spatial interlocking structure". Rheology and SEM techniques were used to determine the optimal conditions for the preparation of the core-shell structure. And FTIR, XRD and TGA systems were used to analyze the chemical composition of the core structure. SEM, TEM, XRD, TGA and FTIR are used to verify our proposal of core-shell construction by interpenetrating the core and shell layers to form a "spatial interlocking structure". Physical properties, color stability, retention of ACNs, antioxidant capacity, and active ingredient release and permeation were then used to assess the functional effectiveness of the oral membrane formulations. This work provides new encapsulation methods for hydrophilic actives.

2. Materials and methods

2.1. Materials

'Lanmei 1' blueberry anthocyanins (ACNs) were obtained from Zhejiang Lanmei Technology Co., Ltd. (Zhejiang, China), with total anthocyanins content of 40%. Konjac glucomannan (KGM, ≥95%purity, Mn: 809,473 g/mol, Mw: 854,507 g/mol, Viscosity, ≥35000 mPa s, Moisture≤10%, Acetyl group content: 3.2% Determination of Acetyl Content by Acid-Base Titration, indicating it is native, non-deacetylated KGM), was purchased from Shanghai Macklin Biotechnology Technology Co., Ltd. (Zhejiang, China). Polyvinylpyrrolidone (PVP, Mw: 1,300,000 g/mol, k88-96), was purchased Shanghai Aladdin Biochemical Technology Co., Ltd. (Shanghai, China). Poly (vinyl alcohol) (PVA, Mw: 145,000 g/mol, the degree of alcoholysis is 98%-99%). was purchased from Shanghai Macklin Biotechnology Technology Co., Ltd. (Zhejiang, China). MTT was purchased from Beijing Solarbio Science & Technology Co., Ltd. (Beijing, China). Pig's tongue (purchased at local market).

2.2. Coaxial electrostatic spinning solution preparation

The nucleoid solution was prepared as follows: PVP (5%, 10%, and 15% w/v) and KGM (2%, 4%, and 6% w/v) were respectively dissolved in distilled water, followed by continuous stirring using a magnetic stirrer for 3 h until complete dissolution. Subsequently, ACNs (0.1%, 0.2%, and 0.4% w/v) were added to the above PVP/KGM mixed solution, and stirring was continued for 10-15 min. Finally, the solution was left to stand and underwent a de-bubbling treatment to eliminate interference from air bubbles in subsequent experiments.

The shell-type electrostatic spinning solution was prepared as follows: PVA (15% w/v) was weighed and dissolved in an appropriate amount of deionized water. Stir with a magnetic stirrer at 70 °C for 4 h until complete dissolution. Wait until a homogeneous, viscous PVA solution was obtained. Transfer to room temperature and leave to stand for defoaming treatment. To eliminate the interference of air bubbles inside the solution to the subsequent experiments.

2.2.1. Coaxial electrostatic spinning parameters

The shell and core fluids were placed in separate syringes. The syringes were connected to an 18-gauge needle, and then a 16-gauge needle was connected to a coaxial needle (0.35 mm ID, 1 mm OD) through a polytetrafluoroethylene wire. The coaxial needle was connected to the positive terminal of the power supply and PVA solution was used as the shell solution. PVP/KGM/ACNs were used as the core solution. The flow rate of the shell solution from the outer coaxial needle was 10 μL/min, and the flow rate of the core solution from the inner coaxial needle was 12 μL/min. The voltage was 18-20 kV, and the distance between the coaxial needle and the collection plate was 10 cm. The fibers were collected on an aluminum foil under the conditions of ambient temperature of 25 ± 5 °C and ambient humidity of 30 ± 10%. In spite of the low ambient humidity, no needle clogging or premature jet termination occurred under the specific conditions of this study, resulting in the successful production of continuous, uniform nanofibers.

2.3. Core structure characterization

2.3.1. Rheological properties

The rheological properties of the spinning solutions were measured using a hybrid rheometer (Discovery HR-1, TA Instruments, USA). Parallel plates with a diameter of 40 mm were selected. The test gap was set to 1000 μm at a temperature of 25 °C, with a shear rate range of 0.01-100 s^{-1}. The steady shear viscosity and stress were recorded during the ramp flow. The dynamic viscoelastic response, including energy storage modulus and loss modulus, was monitored duri ng oscillatory strain and time scans (frequency of 1 Hz) (Bao et al., 2024).

2.3.2. SEM

The morphology of unloaded and loaded ACNs nanofiber membranes was observed by scanning electron microscopy (Hitachi S-4800, Japan). The average diameter of the fibers was measured manually using ImageJ (NIH, USA) with Diameter plug-in. Diameter measurements were

obtained for evaluating fiber diameter, diameter variation and distribution rate of electrospun fibers (Xu et al., 2023).

2.3.3. FTIR

Samples loaded and unloaded with ACNs (PVP, KGM, ACNs, PVP/KGM and PVP/KGM/ACNs) were characterized using an FTIR spectrometer ((Nicolet is 10, Thermo fisher, US). The samples were analyzed at room temperature (22 ± 2 °C) and scans were performed in the spectral range of 4000-500 cm^{-1} (Wen et al., 2018).

2.3.4. Hydrogen nuclear magnetic resonance (^1H NMR)

^1H NMR spectra of Fiber were recorded by using a BRUKER 600 M spectrometer operating at 600 MHz. The Fiber were dispersed in DMSO (20 mg/mL). The dissolved samples were then transferred to NMR tube. Scanning frequency was 0-12 ppm, number of scans was 64.

2.3.5. XRD

The samples (PVP, KGM, ACNs, PVP/KGM, and PVP/KGM/ACNs) were analyzed by XRD diffraction (XRD) using an X-ray diffractometer (D8 Advance, Bruker, GmbH, China). The samples were scanned from 5 to 90°(2θ) at a scan rate of 10°(2θ)/min, voltage of 40 kV and current of 40 mA (Li et al., 2021).

2.3.6. Thermogravimetric (TGA)

The samples (ACNs, PVP/ACNs and PVP/KGM/ACNs) were TGA to investigate their thermal degradation behavior on a thermogravimetric analyzer (METTLER TOLEDO, Switzerland), with a ramp rate of 10 °C/min and heating from 25 °C to 600 °C under nitrogen.

The same samples (ACNs, PVP/ACNs and PVP/KGM/ACNs) were scanned using differential scanning calorimetry (DZ-DSC300C, China) to study the variation process of the thermal flow power difference between the sample end and the reference end with temperature or time. The heating rate was 10 °C/min, and the nitrogen heating temperature was from 25 °C to 500 °C.

2.4. NFM structural characterization

2.4.1. Characterization of NFM morphology

The morphology of coaxial nanofiber membranes was observed by scanning electron microscopy according to method 2.3.2. The copper grid was fixed on the collector before electrostatic spinning. When a thin layer of fiber was observed on the copper grid, the copper grid was removed, and the copper grid was placed on a TEM stage to observe the shell-core structure of the coaxial nanofibers by TEM (accelerating voltage of 100 kV, magnification of 10,000 times) (HT7800, Hitac).

2.4.2. NFM structural characterization

Samples (PVA, PVP, KGM, ACNs, PVP@PVA, PVP/KGM@PVA and PVP/KGM/ACNs@PVA) were chemically characterized by FTIR, XRD, 1H NMR and TGA according to Methods 2.3.3-2.3.6.

2.5. NFM physical properties

2.5.1. Tensile and fracture rates

The tensile strength (TS) and elongation at break (EAB) of the films were measured using an electronic tensile machine (GBH-4A, China), and the methodology followed the outlined method with minor adjustments. Film strips (100 mm × 15 mm) were attached to the tester at room temperature with an initial clamping distance of 55 mm to establish a tensile rate of 150 mm/s. Each sample was tested a total of 10 times (Bao et al., 2024). The equations for TS and EAB are as follows (1)-(2):

$$\text{TS(MPa)} = \text{Force at break(N)/Width(mm)} \times \text{Thickness(mm)} \quad (1)$$

$$\text{EAB (\%)} = \text{Elongated length(mm)/Initial length(mm)} \times 100\% \quad (2)$$

2.5.2. Thickness

The thickness of the oral membrane was measured with a vernier caliper, and 10 points of measurement were taken for each sample (Bao et al., 2024).

2.5.3. Disintegration rate

The prepared NFM was cut into a rectangle of 5 cm × 2 cm and placed in a Petri dish. 200 μL of water was dropped on the surface of the oral membrane. The time required for disintegration and pore formation was quantified as disintegration time for each sample. The determination was repeated 10 times for each sample (Bao et al., 2024).

2.5.4. Water contact angle

The hydrophilicity of the nanofiber membranes was evaluated using a contact angle tester. The groups of nanofiber membranes were cut to appropriate sizes to be fixed in a sample holder, and the water contact angle of each group of nanofiber membranes was tested using a water contact angle meter.

2.5.5. Hydrophilicity

The water solubility of the films was determined according to Bao method (Li et al., 2022). films of constant mass were prepared by oven baking at 105 °C, soaked in 50 mL of distilled water for 24 h, and then oven baked at 105 °C until the mass was constant and weighed (Li et al., 2022). Water solubility formula (3).

$$\text{Water solubility (\%)} = \frac{W_1 - W_2}{W_1} \times 100\% \quad (3)$$

where: W_1 is the initial weight of the film (g); W_2 is the weight of the film after soaking and drying (g).

2.5.6. Adhesion property

In order to evaluate the adhesion properties of the NFM, in this study, pig tongue and pig skin were used as the substrate materials to simulate the oral mucosa, and the adhesion properties of the orosoluble film on the above substrate were verified by applying a slight flow of water in order to simulate the flow environment of saliva in the oral cavity (Zhang et al., 2022).

2.6. Potential applications of NFM

2.6.1. NFM stability evaluation

The retention and chromaticity of oral membrane-forming ACNs were determined. The retention of ACNs and color difference (ΔE value) of the oral films after 8 d of light irradiation were also examined. Before determining the amount of ACNs in the oral films, the films were completely dissolved in a pH = 3 buffer solution (Tan et al., 2018).

The retention rate of ACNs was calculated from the following equations (4)–(6).

$$A = pH_{1.0}(A_{520nm}\text{-}A_{700nm})\text{-}pH_{4.5}(A_{520nm}\text{-}A_{700nm}) \quad (4)$$

$$C_{ACNs}(mg/mL) = A*DF*Mr/\varepsilon*L \quad (5)$$

$$\text{Retention rate (\%)} = \frac{C_t}{C_0} \times 100\% \quad (6)$$

where the ACNs content indicates the equivalent of cyanidin-3-glucoside (C3G), A represents the absorbance value of samples, and *DF* means the dilution ratio. The relative molecular mass (*Mr*) of C3G is 449.2 $g{\cdot}mol^{-1}$. ε denotes the molar absorptivity (26900). *L* means path length (1 cm). C_t and C_0 are the ACNs content at time *t* and 0, respectively.

The value of ΔE is calculated by the following formula (7):

$$\Delta E = \sqrt{(L - L0)^2 + (a - a0)^2 + (b - b0)^2} \quad (7)$$

where L, a and b are the lightness, redness-greenness and yellowness-blueness of the composite systems, respectively; L0, a0 and b0 are the color parameters at the beginning (0 d).

2.6.2. NFM antioxidant activity

The orally soluble membrane was dissolved in a buffer solution at pH 3, and the scavenging ability for DPPH and ABTS radicals was determined to comprehensively evaluate its antioxidant capacity (Bao et al., 2024).

DPPH assay: 100 μL of sample solution was mixed with DPPH·anhydrous ethanol solution (0.2 mM, 100 μL) and placed in the dark for 30 min. The absorbance of the samples at 517 nm was measured and assessed for DPPH radical scavenging activity:

$$\text{DPPH}\cdot \text{ radical scavenging activity } (\%) = \left(1 - \frac{A - A_0}{C - C_0}\right) \times 100\% \quad (8)$$

where A is the absorbance of DPPH· + sample; A_0 is the absorbance of sample + ethanol; C is the absorbance of DPPH + ethanol; C_0 is the absorbance of ethanol.

$ABTS^{\cdot+}$ assay: ABTS was dissolved in PBS (0.01 M, pH 7.4) and configured as a 7 mM solution of ABTS, which was reacted with potassium sulfate (final concentration 2.45 mM) to form ABTS, at room temperature and protected from light for 16 h. The ABTS solution was diluted with PBS until the absorbance at 734 nm was 0.70 ± 0.02, and was equilibrated for 30 min for use in the experiment. 100 μL of the sample solution was mixed with 150 μL of ABTS solution and left in the dark for 20 min the absorbance of the sample at 734 nm was measured to assess the free radical scavenging activity of *ABTS*:

$$ABTS^{+} \text{ radical scavenging activity } (\%) = \left(1 - \frac{A - A_0}{C - C_0}\right) \times 100\% \quad (9)$$

where A is the absorbance of $ABTS^{\cdot+}$ + sample; A0 is the absorbance of PBS + sample; C is the absorbance of ABTS + ethanol; C0 is the absorbance of PBS + ethanol.

2.6.3. NFM release in vitro

The release behavior of ACNs was verified by in vitro release experiments. NFM containing ACNs were added to 20 mL of artificial saliva solution (pH 6.8) and incubated on a water-bath shaker (THZ-82, LICHEN, China) at 37 °C, 150 rpm. A 1 mL sample was taken at pre-set 5, 10, 15, 30, 45, 60, 90, 120 min and replaced with an equal volume of fresh artificial saliva(Bao et al., 2024). The release of ACNs at different time points was determined according to Eqs. (3)–(5).

2.6.4. NFM penetration in vitro

Porcine oral tissues are considered to be closer to human oral mucosa than other animal tissues and were therefore used for the in *vitro* drug penetration assay. Mucosa was affixed in a Franz cell (receiving a volume of 15 mL), and the orosoluble film was gently pressed onto the mucosal surface at 37 °C, moistened with artificial saliva (1 mL). The patches were removed at pre-determined times and 1 mL of receptor buffer sample solution was collected and replaced with an equal volume of PBS solution (Zhang et al., 2022). The amount of ACNs permeated through the mucus at different time points was determined according to equations (3)–(5). The antioxidant capacity after permeation was calculated according to 2.6.2.

2.7. Cytotoxicity

The effect of samples on the viability of *Caco-2* cells was determined using MTT assay. 100 μL of cells (cell density of 1 × 105 cells/mL) were inoculated in 96-well dishes and incubated for 24 h. The medium was aspirated and washed with PBS, and then 125 μg/mL of sample was added to each well. The incubation was continued at 37 °C for 24 h and 48 h. The absorbance of each well at 490 nm was determined using an enzyme meter.

2.8. Statistical analysis

The experimental data was presented as a mean value ± standard deviation of triplicate measurement (n = 3). Statistical analysis was performed using GraphPad Prism software (version 10. 0, USA). One-way ANOVA was used. Significance levels labeled $^{*}P < 0.05$, $^{**}P < 0.01$, and $^{***}P < 0.001$, were used to represent significant differences.N. S. was used to indicate no significant difference.

3. Results and discussion

3.1. Core structure evaluation

3.1.1. Rheological properties of core solutions

Rheological analysis helps to understand the fluidity and stability of the spinning solution and to screen the optimal substrate concentration to develop the desired coaxial structure and is an important indicator of coaxiality. The rheological properties of the analyzed nuclear solutions under shear are shown in Fig. 1A. In the experimental results shown in Fig. 1B–D, it can be observed that the viscosities of different concentrations of PVP solutions significantly increase with the increase of their concentrations. Meanwhile, it is noteworthy that the value of G″ is higher than that of G′, indicating that the samples exhibit predominantly viscous behavior rather than elastic solid-like characteristics (Akcicek et al., 2024). In Fig. 1F–H, it is noteworthy that the rheological behavior (G″ > G′) observed here differs from the strong elastic physical entanglement (G′ > G″) typically reported for deacetylated KGM systems under static conditions. This discrepancy can be attributed to the use of native (acetylated) KGM in the present study. The preserved acetyl groups hinder extensive chain alignment and hydrogen-bond-driven gelation, resulting in a viscous-dominant fluid that is, however, favorable for electrospinning by providing sufficient chain entanglement for fiber formation while maintaining jet stability. This is mainly due to the thickening effect of KGM as well as the interaction generated between PVP and KGM. It is worth noting that G″ is consistently higher than G′ across the tested range, confirming that the system behaves as a viscous liquid rather than an elastic gel (Dodero et al., 2019).

Fig. 1G–I, M shows the loss factor which indicates that the material is elastic or viscous. From the figure, it is concluded that the loss factor increases with the addition and content of KGM and ACNs, indicating that the liquid has a stronger fiber-forming behavior. Fig. I, M shows a significant increase in loss factor with the addition of different concentrations of KGMs and ACNs and remains consistent across a range of shear strains, indicating an increase in chain entanglement and cross-linking. This core solution exhibits predominantly viscous behavior, dissipating mechanical energy as heat rather than storing it elastically. The enhanced structural stability contributes to the formation of uniform nanofibers free of bead defects during electrostatic spinning, supported by a strong network of crosslinked chains capable of forming nanofibers continuously (Lan and Lai, 2023).

Fig. J-L After high shear, while determining the content of PVP and KGM. the concentration of ACNs increased. The decrease in G′ following the addition of ACNs suggests that ACNs may interfere with the alignment of polymer chains. However, viscous dissipation remains dominant in this system (G″ > G′), which is conducive to the formation of a stable jet during electrospinning. In summary, differences in G″ and G′ values reflect changes in polymer chain entanglement and interactions, which influence the viscoelastic and spinnability of the solution (Ma and Chen, 2025). This suggests the ability to derive the optimal matrix concentration required to form the desired core structure in the fabrication of PVP/KGM/ACNs. Meanwhile, we found that KGM, PVP and ACNs

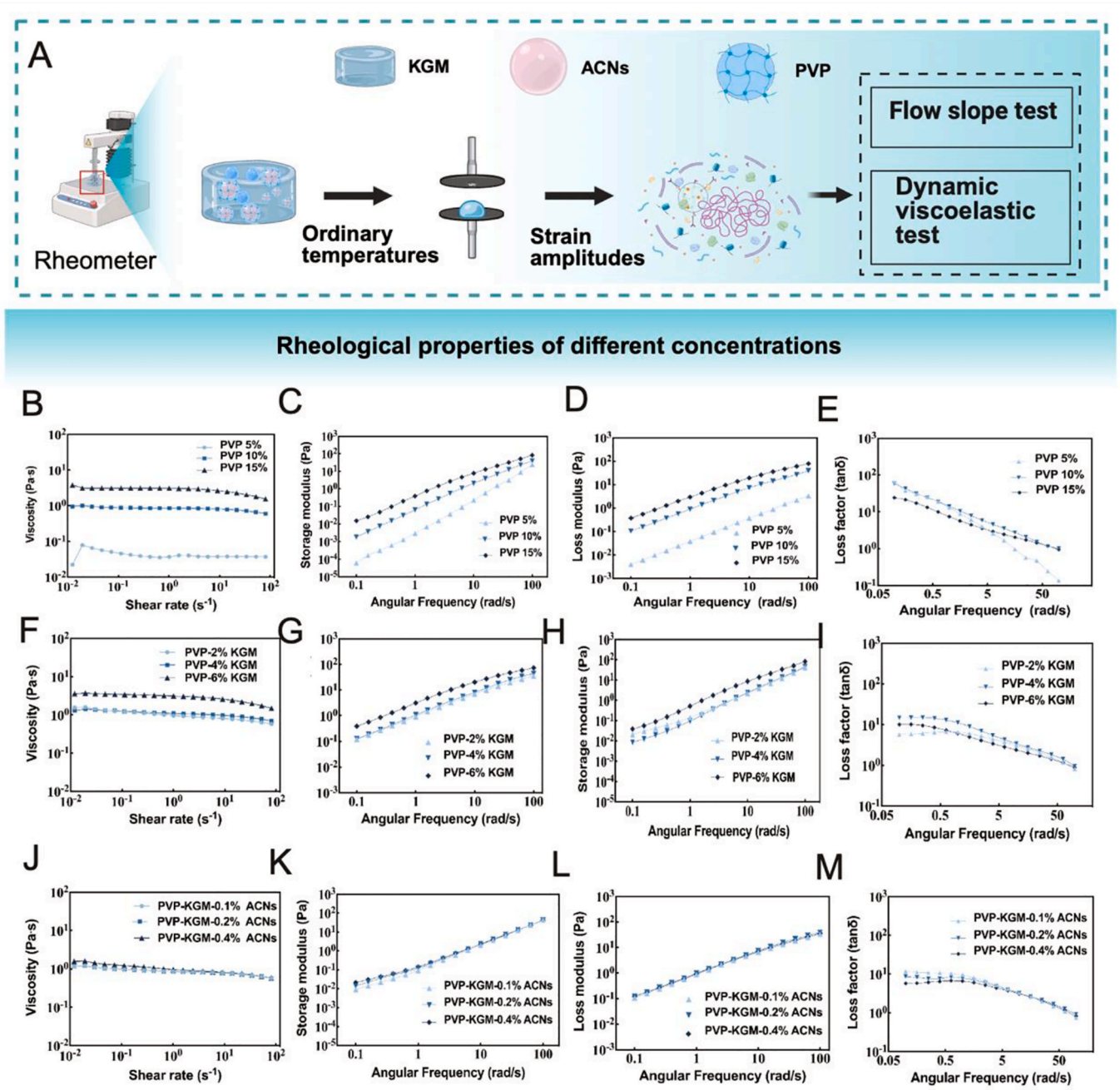

Fig. 1. Effect of different concentrations on apparent viscosity, dynamic viscoelasticity and alternating strain scans of oral membranes. presents a schematic diagram of the rheological tests(A) Created with BioRender.com. The rheological profiles of different substance combinations PVP (10%, 15%, 20%w/v); PVP/KGM (0.2%, 0.4%, 0.6%w/v) PVP/KGM/ACNs (0.1%, 0.2%, 0.4%w/v) are presented in the figure. Specifically, they include viscosity (B, F, L), energy storage modulus (C, G, K), and loss modulus (D, H, L), as well as loss factor (E, I, M). where the energy storage modulus and the loss modulus are denoted by G' and G'' respectively.

formed a composite core layer, which depended on the intermolecular hydrogen bonding between PVP and KGM to enhance the solution viscoelasticity and fiber-forming stability.

It is noteworthy that the rheological behavior of the system studied here differs from that commonly observed in deacetylated KGM gel systems in the literature. Since this study employs non-deacetylated KGM, it exhibits a viscous-dominant characteristic with $G'' > G'$, which is more conducive to electrospinning jet stability and continuous fiber formation. Given the use of low-concentration non-deacetylated KGM and the absence of significant thermal treatment during electrospinning, the thermally induced gelation behavior reported in deacetylated KGM systems does not apply to this system.

3.1.2. *Core structure SEM analysis*

SEM images and histograms of average fiber diameter distribution of PVP, PVP/KGM and PVP/KGM/ACNs-based nanofibers with different concentrations are given in Fig. 2. In the electrostatic spinning process, the solution viscosity reflects the degree of polymer chain entanglement, which is the key to fiber spinnability, morphology and spinning success. Fig. 2A–C shows that the fiber diameter increases with increasing PVP concentration, with average diameters of 0.16 ± 0.01 μm, 0.78 ± 0.26 μm, 1.71 ± 0.25 μm, respectively (Fig. 2 A1-C1). Where Fig. A and C, on the one hand, the increase in conductivity leads to an increase in electrostatic force and Coulomb repulsion, which leads to an increase in the elongation of the jet along its axial direction and produces fine nanofibers that can lead to difficult load ACNs (Dharmansh,

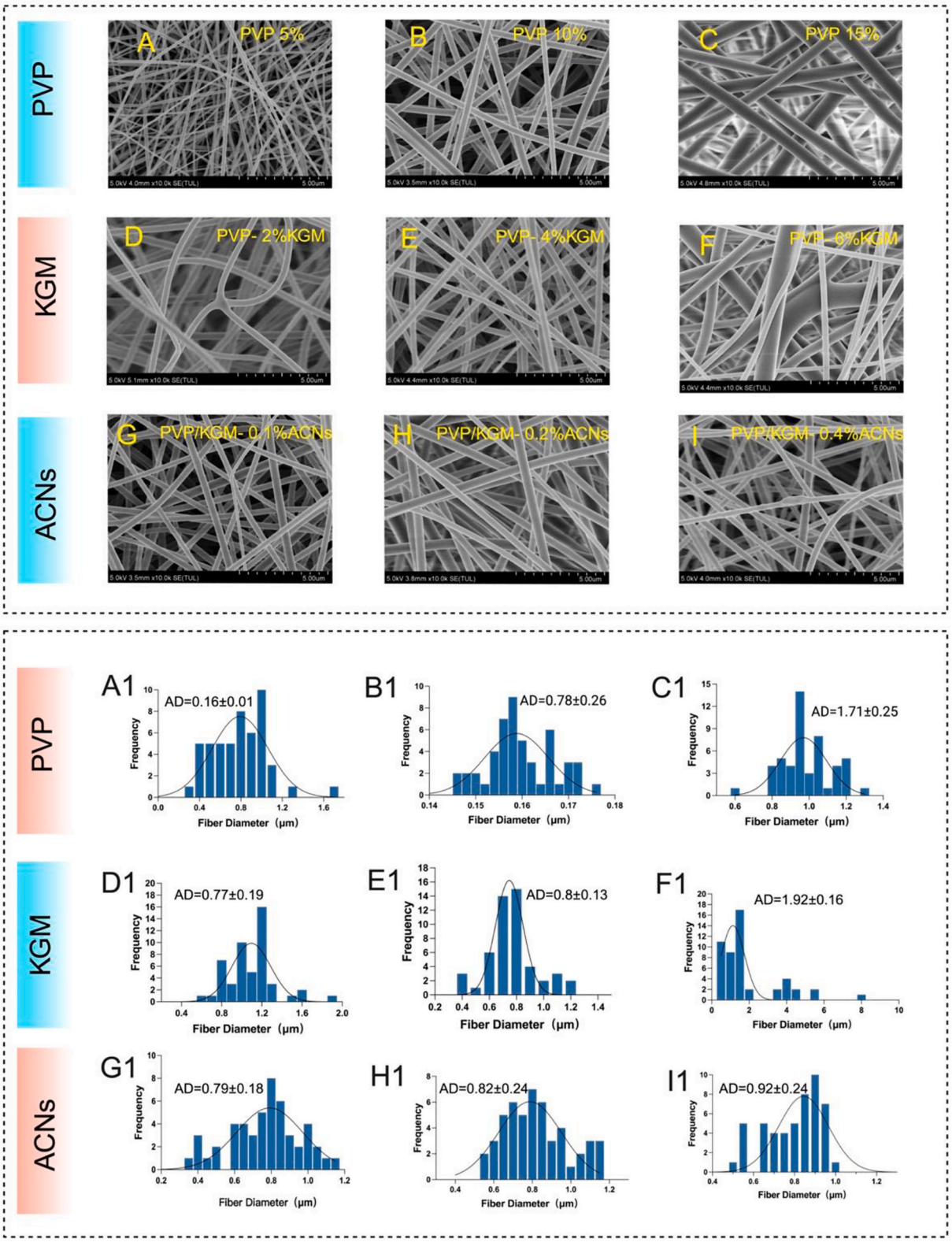

Fig. 2. Schematic diagram of the morphological analysis of core structure. SEM images of nuclear-structured nanofibers prepared with different solution concentrations PVP 5%, 10%, 15%w/v(A-C); PVP/KGM 2%, 4%, 6%w/v (D-F); PVP/KGM/ACNs 0.1%, 0.2, 0.4%w/v(G-I). Diameter distribution images of core-structured nanofibers prepared at different solution concentrations PVP 5%, 10%, 15%(A1-C1); PVP/KGM 2%, 4%, 6% (D1-F1); PVP/KGM/ACNs 0.1%, 0.2, 0.4% (G1-I1).

2018). On the other hand, the increase in viscosity enhances the entanglement between the chains, resulting in thicker nanofibers. Based on the comprehensive analysis of fiber morphology characteristics and process feasibility, 10% PVP was selected as the crosslinker concentration (Lu et al., 2021).

While KGM incorporation plays a protective role for ACNs to improve the stability of ACNs. In Fig. 2D–F when PVP/KGM composite, KGM concentration of 2% and 6% showed beaded rough fiber

morphology. This may be due to the change in the morphology of taylor cone by too much concentration of KGM during the electrospinning process resulting in the structure and morphology of the fibers being affected. Smooth, homogeneous fiber morphology is observed in Fig. 2E. This apparent difference in morphology stems from the difference in polysaccharide concentration. The reason may be attributed to polymer chain entanglement due to functional group interactions between PVP and KGM, which is consistent with the rheological results. Therefore, Fig. 2E was chosen as the nuclear carrier loaded with ACNs. Fig. 2G–I, different concentrations of ACNs were added. in contrast, 0.1% and 0.4% concentrations of ACNs spun out unevenly thick and bumpy fibers. It indicates that the ACNs were not completely encapsulated. This could be a result of migration of the material during electrostatic spinning, thus affecting the morphology. In addition, we observed smooth fibers in Fig. 2H. This finding suggests that the ACNs were successfully incorporated into the nanofiber matrix. The smooth surface of the core fibers reduces friction and wear, and at the same time, it helps to improve the interfacial bond strength between the core and shell layers, ensuring the overall stability of the composite. Based on quantitative analysis of scanning electron microscope images, a systematic statistical analysis was conducted on fiber diameter distribution, bead defect rate, and coefficient of variation (CV). Results indicate that under the conditions corresponding to Fig. 2H (PVP 10% w/v, KGM 4% w/v, ACNs 0.2% w/v), the prepared nanofibers exhibited optimal comprehensive morphological characteristics: an average diameter of 1.38 ± 0.27 μm, the lowest diameter coefficient of variation (CV = 12.5%), and a bead defect ratio below 5%. In contrast, other experimental groups exhibited either pronounced bead structures or uneven diameter distributions (CV > 20%). Therefore, based on quantitative criteria of high diameter uniformity and low defect rate, this condition was identified as the optimal core layer composition and employed for subsequent coaxial electrospinning to prepare core-shell structured nanofiber membranes (NFM). Therefore, Fig. 2H was chosen as the nuclear structure for subsequent experiments.

3.1.3. FTIR analysis

The interaction between ACNs and PVP/KGM membrane matrix was characterized by FTIR spectroscopy as shown in Fig. 3A. In the ACNs spectra, it was found that the characteristic peaks of ACNs vibration in the aromatic ring of benzopyran were monitored at 1654 cm^{-1}, 1660 cm^{-1} and 1365 cm^{-1} (C-C ring stretching), which is typical of flavonoid derivatives (Bao et al., 2024; Zhang et al., 2024). After the addition of ACNs to PVP/KGM, it was observed that the -OH peak was found to move to a lower wave number with the O-H of free ACNs. This may be due to the strong interaction between ACNs and PVP/KGM. In addition, a shift of the C-O-C stretching band from 925 cm^{-1} to 921 cm^{-1}, which is the characteristic absorption peak of the mannose unit in KGM, was pointed out, which can be attributed to the vibration of the backbone C-C and the presence of β-1,4 glycosidic bonds (Chen et al., 2024). In the FTIR spectra of KGM and its composites, a characteristic absorption peak at approximately 1730 cm^{-1} was observed, corresponding to the C=O stretching vibration of the acetyl group. Notably,

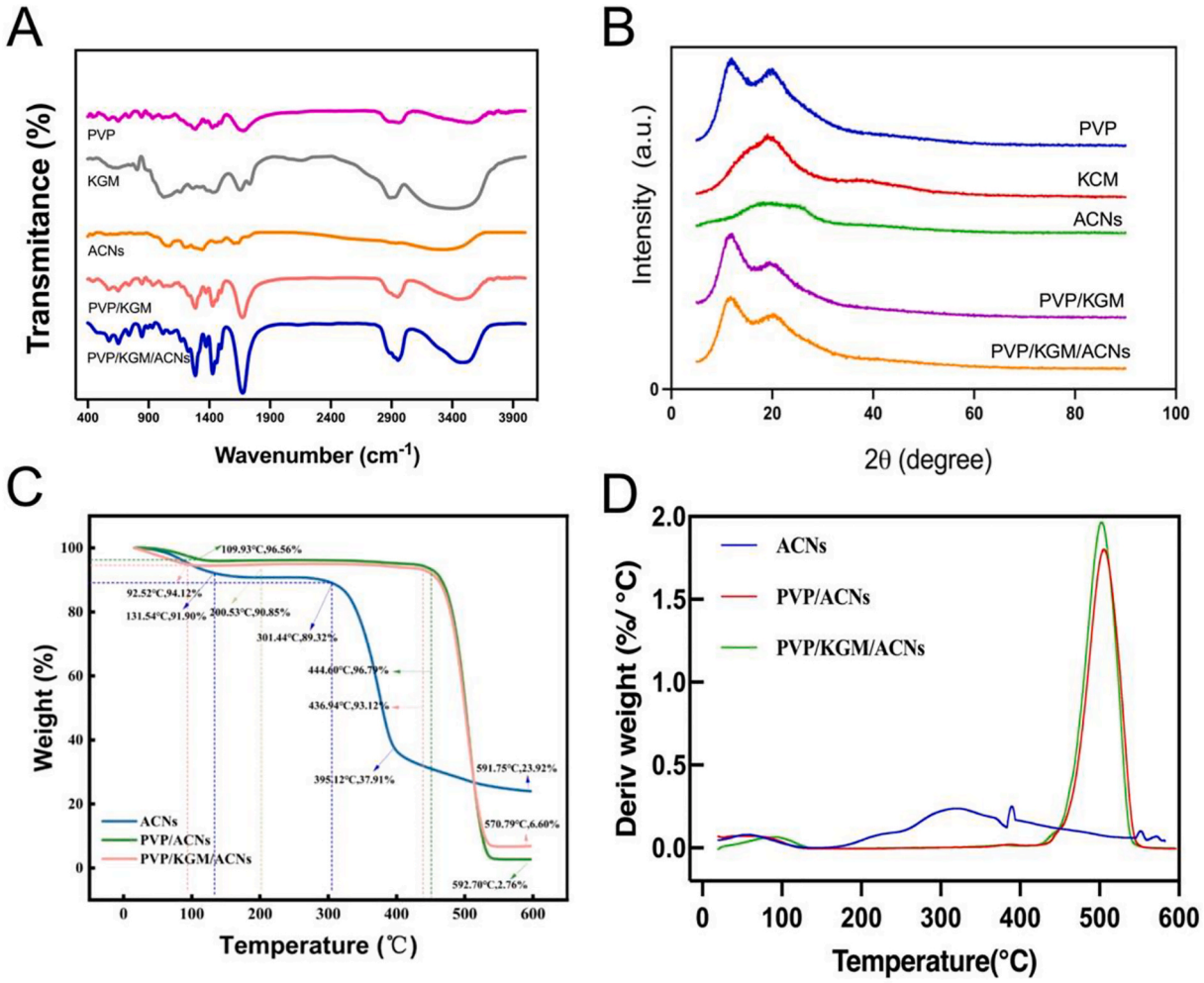

Fig. 3. (A) FTTR spectra of PVP, KGM, ACNs PVP/KGM, PVP/KGM/ACNs. (B) XRD spectra of PVP, KGM, ACNs PVP/KGM, PVP/KGM/ACNs. The TGA (C) and DTG (D) curves of ACNs PVP/KGM, PVP/KGM/ACNs.

deacetylation in KGM-based systems may introduce hydrophobic interactions that promote polymer aggregation. However, since un-deacetylated KGM was used in this study, such hydrophobic effects are expected to be limited and cannot be distinguished from hydrogen bonding interactions in FTIR analysis. Thus, interactions within the PVP/KGM/ACNs system originate not only from hydrogen bonding (The position of O-H peak moved from 3448 cm^{-1} to 3443 cm^{-1}, which suggested that it might be intermolecular hydrogen bond interaction (Fig. S2).), However, the relatively small peak shift magnitude may be attributed to physical mixing effects), but also involve the contribution of acetyl groups in maintaining the liquid stability of polymer chains. This composite interaction mechanism effectively prevents the formation of rigid, viscous structures, thereby facilitating the implementation of the electrospinning process. It is noteworthy that the characteristic peaks of ACNs complexed with PVP/KGM were masked, suggesting a more complete binding of ACNs, which is consistent with the SEM results.

3.1.4. ^1H NMR spectroscopy analysis

To further validate the intermolecular interactions proposed by FTIR analysis, ^1H NMR spectra of the core layer ACNs, KGM/PVP, and KGM/PVP/ACNs were analyzed (Fig. S3) The ACN spectrum exhibits multiple sharp signals in the 3.0-5.5 ppm range, corresponding to sugar units and hydroxyl protons on the anthocyanin skeleton. KGM/PVP exhibits characteristic broad peaks characteristic of the polymer matrix. Signals at 1.2-2.4 ppm are attributed to methylene protons on the PVP backbone and pyrrolidone rings. The overlapping peaks in the 3.2-4.5 ppm region correspond to the methylene/methylene protons of the KGM sugar units and the N-methylene protons of PVP. Upon incorporation of ACNs into the matrix, the proton signal underwent changes. In the composite membrane spectrum, the original peak of free ACNs exhibited slight broadening. This phenomenon indicates that the molecular motion of ACNs is restricted in the KGM/PVP matrix. This indicates that the interaction between ACNs and the polymer chain achieves dispersion and immobilization at the molecular level. Detailed comparison of the 3.0-5.0 ppm region (corresponding to hydroxyl and sugar rings) reveals slight chemical shifts and broadening of spectral lines. These changes are attributed to the formation of intermolecular hydrogen bonds. The phenolic hydroxyl group of ACNs acts as a hydrogen bond donor, interacting with the carbonyl group (C=O) of PVP and the hydroxyl group (-OH) of KGM. This interaction alters the electron density around the proton, leading to the observed spectral changes. The ^1H NMR results provide molecular-level evidence that ACNs are successfully encapsulated within KGM/PVP fibers driven by hydrogen bonding interactions.

3.1.5. XRD analysis

The crystalline properties of the nuclear structures were characterized by XRD analysis to explain the molecular compatibility between the components. As shown in Fig. 3B, the diffraction pattern of ACNs showed broad diffraction peaks in the range of $2\theta = 15°$-$28°$, indicating semi-crystalline properties. It is noteworthy that when PVP is complexed with KGM, the intensity of the characteristic diffraction peaks at $2\theta = 12°$ and $2\theta = 20°$ is weakened compared with that of the single-component PVP and KGM, which is attributed to the formation of intermolecular interactions (e.g., hydrogen bonding or electrostatic force), which disrupts their original crystalline regions (J. Wang et al., 2025). Interestingly, after introducing ACNs into the PVP/KGM matrix, the distinct diffraction features of ACNs almost disappeared, and no new crystalline phases were observed. This suggests that the ACNs may be dispersed in the nanofibrous structure in an amorphous state. DSC analysis further supported the amorphous dispersion of ACNs (Fig. S4). No distinct melting endotherm corresponding to crystalline ACNs was observed in the DSC thermogram of the PVP/KGM/ACNs nanofibers, indicating that ACNs were not present in a crystalline state but were dispersed in an amorphous or molecularly distributed form within the nanofibrous matrix.

3.1.6. TGA analysis

Thermogravimetric analysis can be used to evaluate the closeness of the interactions between the nucleation matrices, as shown in Fig. 3C–D. The mass loss process for all samples can be broadly divided into three stages. The slight weight loss (~5%) observed in the first stage (approximately 25-100 °C) is primarily attributed to the evaporation of bound water within the samples. The second stage (100-400 °C) represents the region where the polymer backbone and active components undergo primary thermal decomposition. During this stage, free ACNs exhibited the fastest decomposition rate and the greatest cumulative mass loss (42.09%). Notably, the DTG curve (Fig. 3D) provides a more precise basis for comparing thermal stability. The main initial decomposition temperature (T_d) of free ACNs is 312 °C. When ACNs is blended with PVP (PVP/ACNs), its melting point rises to 510 °C. The T_d of PVP/KGM/ACNs further increased to 514 °C. Consistent with the DTG trend, the TGA curve revealed that within this temperature range, the mass loss rates of PVP/ACNs and PVP/KGM/ACNs (3.02% and 6.88%, respectively) were significantly lower than that of free ACNs. This confirms the protective effect of the PVP matrix on ACNs. The incorporation of KGM forms a more stable composite network through intermolecular interactions with PVP and ACNs, thereby synergistically enhancing the thermal stability of the system (Li et al., 2023). The third stage (400 - 600 °C) corresponds to the slow carbonization process of the residue.

After determining the optimal film-forming ratios by rheological and morphological analysis. Then, the tight binding achieved by the interaction between the composite systems was verified by FTIR, XRD and TGA, and subsequently we used the screened optimal ratio of nuclear fibers to prepare the coaxial structure.

3.2. NFM structure characterization

3.2.1. Morphological characteristics of NFM

Electrostatically spun membranes with core-shell structure loaded with ACNs were prepared by coaxial electrostatic spinning using PVP, KGM, ACNs as the core layer substrate and PVA as the shell layer substrate as shown in Fig. 4A–C. The surface of the fiber shows a smooth and uniform quality, with no holes, beads, cracks or other imperfections. In this study, the diameter of PVP/KGM@PVA coaxial nanofibers is 0.98 ± 0.13 μm (Fig. 4A1), and the fiber diameter increases with the addition of KGM core ACNs. The diameter of PVP/ACNs@PVA nanofibers with PVP/ACNs as the core material is 1.09 ± 0.12 μm (Fig. 4B1). When KGM and ACNs are core materials, the diameter of PVP/KGM/ACNs@PVA fibers is 1.38 ± 0.27 μm (Fig. 4C1). From the results, it was concluded that the coaxially prepared fibers were uniform. In order to verify whether the fibers prepared from 15% PVA shell solution and core solution have coaxial shell-core structure, we observed their microstructures by TEM. Fig. 4D–F shows the transmission electron microscope images of the electrospun fibers. The electrospun fibers have an obvious shell-core structure with a black middle layer and a gray outer surface. It indicates that the coaxial electrospun fibers were successfully prepared by the successful incorporation of ACNs into the nanofiber matrix, which further validates the SEM results. The distinct core-shell structure observed by TEM indicates that phase separation occurred between KGM and PVA during preparation. However, the formation of this structure is not a simple thermodynamic equilibrium process. We propose that KGM preferentially undergoes gelation in the presence of crosslinking agents or under specific conditions, thereby guiding and freezing this non-equilibrium core-shell morphology.

3.2.2. FTIR analysis

FTIR spectroscopy was performed on the coaxial electrostatically spun films, as shown in Fig. 5A. In the spectrum of PVP@PVA, the typical peaks at 3468 and 1648 cm^{-1} are the presence of amide groups, corresponding to N-H stretching vibrations and C=O stretching

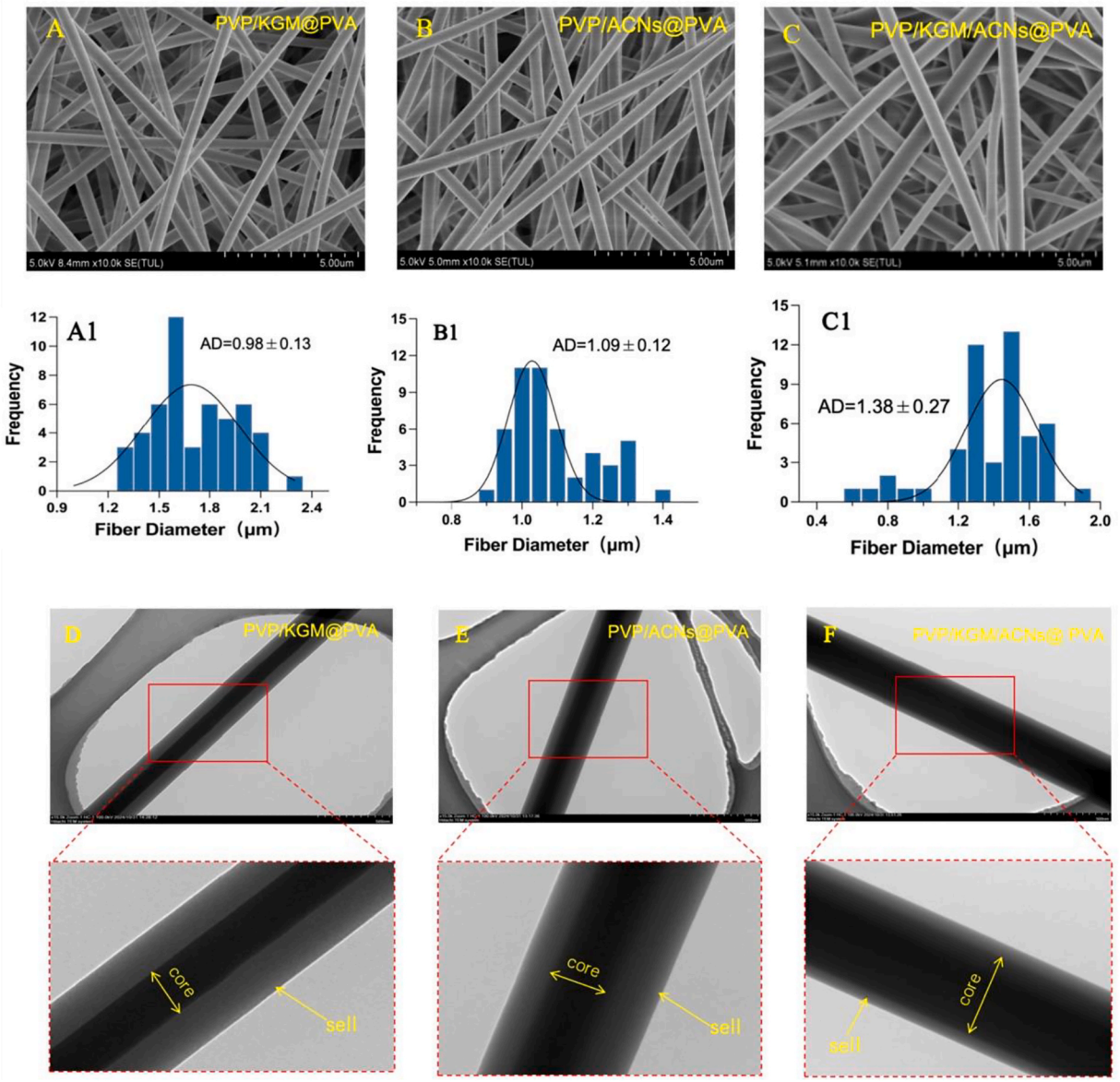

Fig. 4. Schematic diagram of NFM morphological structure analysis. SEM (A-C) and diameter distribution(A1-C1) of coaxial nanofibers prepared by PVP/KGM@PVA, PVP/ACNs@PVA, PVP/KGM/ACNs. TEM (D-F) images of coaxial nanofibers prepared by PVP/KGM@PVA, PVP/ACNs@PVA, PVP/KGM/ACNs.

vibrations, respectively (Amide I band). In addition, the absorption peaks at 1085 cm^{-1}, 1296 and 1465 cm^{-1} are C-O stretching vibrations, which belong to amide I bond, the absorption peak at 1296 cm^{-1} is C-N stretching vibration, and the absorption peak at 1465 cm^{-1} is a shear bending vibration of CH_2. KGM incorporation, PVP/KGM@PVA spectra, the characteristic peaks of KGM were found to be red-shifted towards lower bands. The characteristic peaks were shown at 1293 cm^{-1}, 1463 cm^{-1}, 1693 cm^{-1} and 3468 cm^{-1} for C-O stretching vibration, shear bending vibration of CH_2, C=O stretching vibration and -OH stretching vibration, respectively. In the FTIR spectra of the PVP@PVA and PVP/KGM/ACNs@PVA systems, a prominent broad absorption band appears at ~3468 cm^{-1}. This peak is attributed to the O-H stretching vibration of hydroxyl groups abundant in the PVA matrix and KGM. This broad peak is located in the hydrogen-bonded O-H region, suggesting that the hydroxyl group in the system may be in a hydrogen-bond-related environment. To obtain more reliable quantitative evidence (Fig. S5), we performed peak-by-peak fitting in the C=O stretching vibration region (3000-3800 cm^{-1}), decomposing the overall absorption envelope into four component peaks. Among these, high-frequency component peaks correspond to weakly associated C=O environments, while low-frequency component peaks correspond to hydrogen-bonded C=O environments. Compared to PVP@PVA, the incorporation of KGM/ACNs increases the area fraction of the C=O component peak at low wavenumbers while decreasing the relative fraction at high wavenumbers, indicating that carbonyl groups may overall tend toward a hydrogen-bonded association state (Wang et al., 2024). In the spectrum of ACNs, 1624 cm^{-1}, 1634 cm^{-1} and 1365 cm^{-1} monitored the characteristic peaks of ACNs vibration in the aromatic ring of benzopyran (C-C ring stretching), which is typical of flavonoid derivatives. When ACNs were added, the spectral comparison showed that the PVP/KGM/ACNs@PVA spectra did not contain the characteristic peaks of free ACNs, suggesting that the ACNs were encapsulated in coaxial nanosystems, which prevented the loss of ACNs bioactivity due to light and oxidation, but also maintained the sustained release of ACNs. In addition, the width of the hydroxyl stretching bonds was broadened between 3000 and 3500 cm^{-1} due to the increase of hydrogen bonding between ACNs and PVP/KGM@PVA nanofibers (Kazemianrad et al., 2023)。

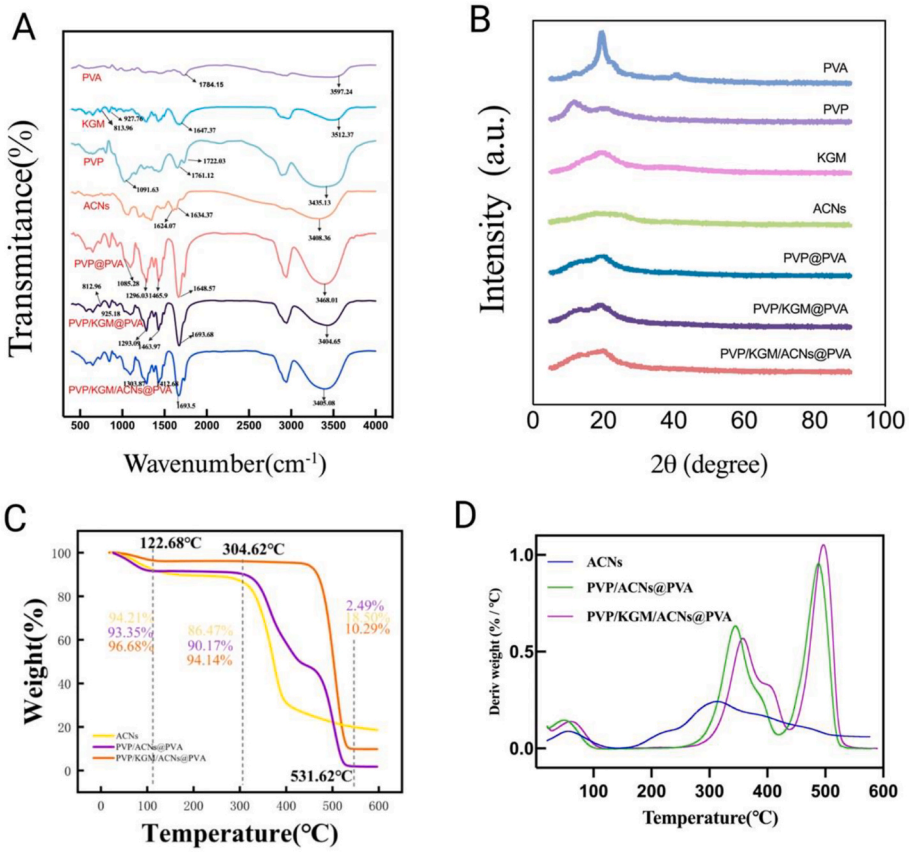

Fig. 5. FTIR (A) and XRD (B) spectra of PVA, PVP, KGM, ACNs, PVP@PVA, PVP/KGM@PVA, PVP/KGM/ACNs@PVA. The TGA (C) and DTG (D) curves of ACNs, PVP/ACNs@PVA, PVP/KGM/ACNs@PVA.

3.2.3. ^{1}H NMR spectroscopy analysis

Nuclear magnetic resonance ^{1}H NMR analysis was performed on ASNs, PVP@PVA, PVP/KGM@PVA, and PVP/KGM/ASNs@PVA (Fig. S6). The ^{1}H NMR spectrum of PVP@PVA exhibits characteristic signals of the polymer matrix. Peaks in the range of 1.2-1.8 ppm are attributed to methylene protons (-CH_2-) in the polymer backbone. The signals at 1.9-2.4 ppm and 3.0-3.2 ppm correspond to the methylene protons on the pyrrolidone ring of PVP. The methylene protons (-CH-) of PVA appear near 3.8-4.0 ppm, while the multi-peak in the 4.0-5.0 ppm region is attributed to the hydroxyl protons (-OH) of both PVA and KGM. When polysaccharide KGM is introduced into the matrix, the primary changes are observed in the region of active hydrogen (4.0-5.5 ppm). Compared to the PVP@PVA spectrum, the PVP/KGM@PVA spectrum exhibits slightly broader signal profiles in the 4.2-5.0 ppm range. This change is attributed to the introduction of a large number of hydroxyl groups into the KGM molecular chain. Crucially, the hydroxyl peak exhibits a tendency toward downfield shift and broadening. This phenomenon indicates a change in the chemical environment of the protons, providing direct evidence for the existence of intermolecular hydrogen bonds. The abundant hydroxyl groups on the KGM skeleton act as hydrogen bond donors, interacting with the carbonyl groups (C=O) of PVP and the hydroxyl groups of PVA. The broadening of the overall proton signal in the spectrum further indicates restricted motion of the polymer chains. This confirms that the incorporation of KGM forms these hydrogen bond interactions, thereby enhancing the compatibility of the NFM system.

3.2.4. XRD analysis

PVP@PVA, PVP/KGM@PVA and PVP/KGM/ACNs@PVA (Fig. 5B), with a broader peak at around 2θ = 20°, 2θ = 19° and 2θ = 21°, respectively. The characteristic x-ray diffraction peak of ACNs has a broader delayed peak at about 2θ = 21° or so, but the peak is flatter, suggesting that ACNs have amorphous structural features at lower crystallinity. As for the PVP/KGM@PVA characteristic diffraction peaks, the peaks become broader and weaker in intensity. The reason for this may be the existence of strong hydrogen bonding interactions between the shell-core, which restricts the movement of the molecular chains within the substance. This limitation leads to more amorphous structures, which reduces the crystallinity of the films. After the addition of ACNs, the characteristic diffraction peaks of ACNs disappeared. This may be due to the interactions between the molecules altering or masking their crystal structure (Wang et al., 2022).

To support the observed weakening of diffraction peaks of ACNs in XRD and further investigate the changes in their crystalline state, we performed DSC analysis on the thin-film samples. As shown in Fig. S7, pure ACNs exhibit a pronounced melting endothermic peak at around 179 °C, indicating that they possess certain ordered structural characteristics. In contrast, for the composite film PVP/KGM/ACNs@PVA, this endothermic peak is significantly weakened or even unobservable. The heat flow curve tends to broaden and lacks typical melting characteristics, indicating that the crystallinity and ordered structure of ACNs are suppressed within the composite system, and no observable long-range ordered structure is presented within the detection range of DSC.

3.2.5. TGA analysis

The thermal stability of coaxial electrospun fibers was analyzed by TGA and DTG (Fig. 5C–D). When the temperature is below 100 °C there is a slight decrease in sample weight during the first minutes of measurement. This effect is related to residual moisture in the fiber membrane and can be clearly distinguished from other mass drops at higher temperatures. A more pronounced decrease in thermal stability of ACNs was observed in the temperature range of 200°C-400 °C. DTG Further

analysis revealed that the initial degradation temperature of the PVP/ACNs@PVA samples was about 230 °C, whereas the PVP/KGM/ACNs@PVA fibrous membranes were more stabilized by the incorporation of polysaccharides to make the component synergistic structure (Wu et al., 2024), the degradation temperature rises to about 300 °C. This can be explained by the shell-core structure in the nanofiber background matrix and by the fact that the carbon layer produced when pyrolysis of polysaccharides starts at around 300 °C can block heat transfer. Heat treatment leads to the decomposition of macromolecules into smaller volatile molecules, so that the sharp decrease in mass at 400°C-500 °C is explained by the carbonization of the sample. The final sample mass reaches an almost constant value which corresponds to the ash content of the sample. In summary, PVP/KGM/ACNs@PVA nanofibers have good thermal stability.

In prepared coaxial structures based on the nuclear fibers screened earlier. We study the coaxial structure in terms of microscopic morphology, crystal orientation and interfacial bonding properties. The results show that the coaxial fibers are smooth and uniform and form a

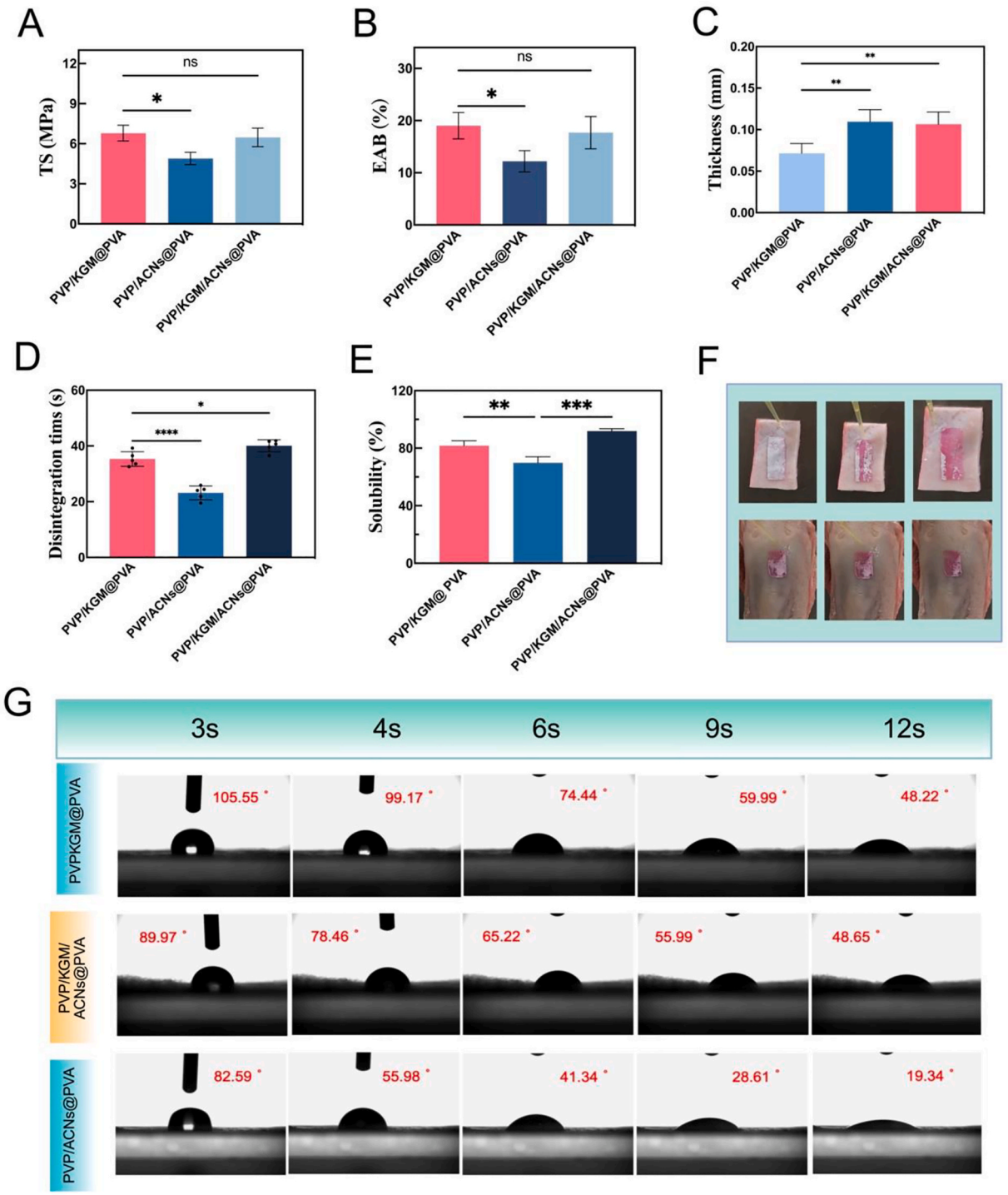

Fig. 6. Physical characterization of NFM. (A) Tensile strength (TS). (B)Elongation at break (EAB). (C)Thickness, (D) Disintegration time. (E)Solubility. (F)Apparent viscosity. (G) PVP/KGM@PVA, PVP/ACNs@PVA, PVP/KGM/ACNs@PVA water contact angle test. Significance levels labeled*$P < 0.05$, **$P < 0.01$, and***$P < 0.001$, were used to represent significant differences.N.S. was used to indicate no significant difference.

core-shell structure. In addition, coaxial fibers were found to bind through hydrogen bonding interactions. The prerequisite for NFM application is to have good physical properties, next we verify the physical properties of the prepared membranes.

3.3. Physical properties of orally soluble films

3.3.1. Tensile and fracture rates

The mechanical properties of the orally soluble film were studied by tensile test. As shown in Fig. 6A–B, the PVP/ACNs@PVA film showed a tensile strength of 4.89 MPa and an elongation at break of 15.53%. This may be because PVP is related to the decrease of double bond density in PVA. In contrast, the tensile properties of the carrier group (PVP/KGM@PVA) and the group loaded with ACNs (PVP/KGM/ACNs@PVA) were significantly improved. This is attributed to the fact that the addition of KGM induced the formation of a dual physical cross-linking network in the system: PVA crystallized by freeze-thawing as the first network, and KGM constructed the second network through hydrogen bonding (although the hydrogen bonding effect is non-covalent, the results indicate that the PVP/KGM@PVA fiber structure is more stable) (Liu et al., 2024). This physical cross-linking action allows the PVP/KGM/ACNs@PVA fibers to bind and interlock to prevent further physical sliding and maintain structural stability. In summary, the mechanical properties of the PVP/KGM/ACNs@PVA orally dissolvable film (tensile strength of 6.48 MPa and elongation at break of 17.68%) were sufficiently robust for practical use (Tan et al., 2022).

3.3.2. Thickness

The excellent physical properties presented by NFM, especially its thickness parameter as a core physical property, are key indicators for assessing the structural stability of this membrane. As shown Fig. 6C, the addition of KGM significantly increased the thickness of the oral membrane ($p < 0.05$). This is related to the nature of the polysaccharide itself, which forms a thinner membrane due to the lower viscosity of PVP/ACNs@PVA, which forms less site resistance with the membrane-forming matrix. KGM is more viscous and may agglomerate when combined with the film-forming substrate, expanding the spatial structure and leading to an increase in the thickness of the oral film (Ran and Yang, 2022). As a result, the PVP/KGM@PVA and PVP/KGM/ACNs@PVA-based orally soluble membranes exhibited larger thickness characteristics, a phenomenon that coincided with the SEM-observed tendency for fiber diameter to increase with the incorporation of polysaccharides and ACNs. Further, the thickness parameter of the orally soluble film directly correlates with its dissolution duration in the oral environment, thus becoming a key physical property for the release rate and oral retention effect.

3.3.3. Disintegration time

The disintegration time of coaxial nanofibers is shown in Fig. 6D. With the addition of KGM and ACNs, the disintegration time of NFM showed an increasing trend. The experimental results showed that the disintegration time of PVP/KGM/ACNs@PVA (40.08 ± 0.47s) was higher than that of PVP/ACNs@PVA (23.14 ± 0.54s) and PVP/KGM@PVA (35.31 ± 0.14s). It is noteworthy that when KGM were introduced into the PVP/ACNs@PVA matrix, the changing pattern of the disintegration time of the orally dissolved membrane was consistent with the membrane thickness results. However, the disintegration time of coaxial nanofibers prepared when polysaccharides and ACNs were added increased. It is possible that ACNs interact with the active sites on the KGM molecular chains by forming multiple hydrogen bonds through the abundant hydroxyl groups on their surfaces, and this synergistic effect enhances the cross-linking density of the polysaccharide-polymer matrix, and also contributes to the formation of a three-dimensional network structure. At the same time, a viscous gel barrier is formed after the NFM comes into contact with the droplets. The gel barrier hinders the penetration of the droplets and therefore also increases the disintegration time of the NFM (Sha et al., 2022)。

3.3.4. Water contact angle analysis

The magnitude of the contact angle is an indicator that characterizes the hydrophilicity or hydrophobicity of the orally soluble film. The smaller the degree of contact angle, the less hydrophobic it is. The contact angle values of the samples are shown in Fig. 6G. Regardless of the composition, the contact angles of all the membranes were less than 90°, indicating that these nanofiber membranes have a high degree of hydrophilicity. The addition of KGM and ACNs to the PVP/ACNs@PVA nanofiber films reduced their contact angles. This phenomenon is attributed to the interaction between polysaccharides and anthocyanins through non-covalent or covalent interactions. Specifically, in the PVP/ACNs@PVA system, the incorporation of KGM increases the hydroxyl (-OH) content of the hydrophilic group. It is noteworthy that although the main chain of KGM is a linear polysaccharide structure, its molecular chain is modified with short branches or side chains in localized regions, and this unique molecular conformation confers a stretching arrangement (Zhang et al., 2024). At the same time, the high molecular weight properties of KGM lead to the formation of a network structure which effectively adsorbs water molecules through hydroxyl groups, thus significantly enhancing the macroscopic hydrophilicity of the material. This means that more hydrophilic groups are exposed, leading to enhanced hydrophilicity of the membrane. The addition of ACNs resulted in a lower contact angle than PVP/KGM@PVA and PVP/KGM/ACNs@PVA, indicating that the addition of ACNs enhanced the hydrophilicity of the nanofiber membranes (Yuan et al., 2023).

3.3.5. Hydrophilicity and viscosity analysis

The results of membrane solubility are shown in Fig. 6E. From the comparison of the results, it was found that the membrane solubility of added polysaccharides and ACNs were 79.71 % and 93.32 %, respectively, which were significantly higher than that of PVP/ACNs@PVA (69.81 %) ($p < 0.05$). Because both KGM and ACNs are water-soluble substances. Carrying out the composite also increases the hydrophilic groups of the orally soluble membrane. At the same time, the abundant hydroxyl groups on the surface form multiple hydrogen bonding interactions with the active sites on the KGM molecular chain, which effectively adsorbs water molecules through the hydroxyl groups, thus significantly enhancing the macroscopic hydrophilicity of the oral soluble membrane (Li et al., 2021). In NFM applications, hydrophilicity enhances mucosal adhesion and solubility for sustained intraoral drug release and enhancement bioavailability. Therefore, the flow-through method was used to study the residence time of electrospun silk film in *vitro*. In the in *vitro* experiments, the electrospun silk film firmly adhered to the pig skin and pig tongue and did not fall off when rinsed with flowing water (Fig. 6F). This work demonstrates that the long-lasting adhesion properties of ACNs achieved by electrospun fiber carriers allow for the construction of sustained release delivery systems, which in turn significantly enhance their bioavailability (Terlau et al., 2024).

3.4. Potential applications of NFM

3.4.1. Stability evaluation

To evaluate the color and content stability of ACNs after film formation. The colorimetric values and retention of ACNs were measured after 8 d of light exposure (with 0 days as a comparison). The results showed that the coaxially structured orally soluble films prepared proved to stabilize the ACNs. The color loss during light exposure was reduced (Fig. 7A). As shown in Fig. 7B, the retention of NFM light for 8 d was 94.28% (2 d), 88.99% (4 d), 84.57% (6 d) and 81.22% (8 d). The good stability of the ACNs was demonstrated. This stability enhancement can be attributed to a dual synergistic mechanism: on the one hand, the sugar KGM added in the kernel forms a tight bond with ACNs through hydrogen bonding, effectively inhibiting the dissociative

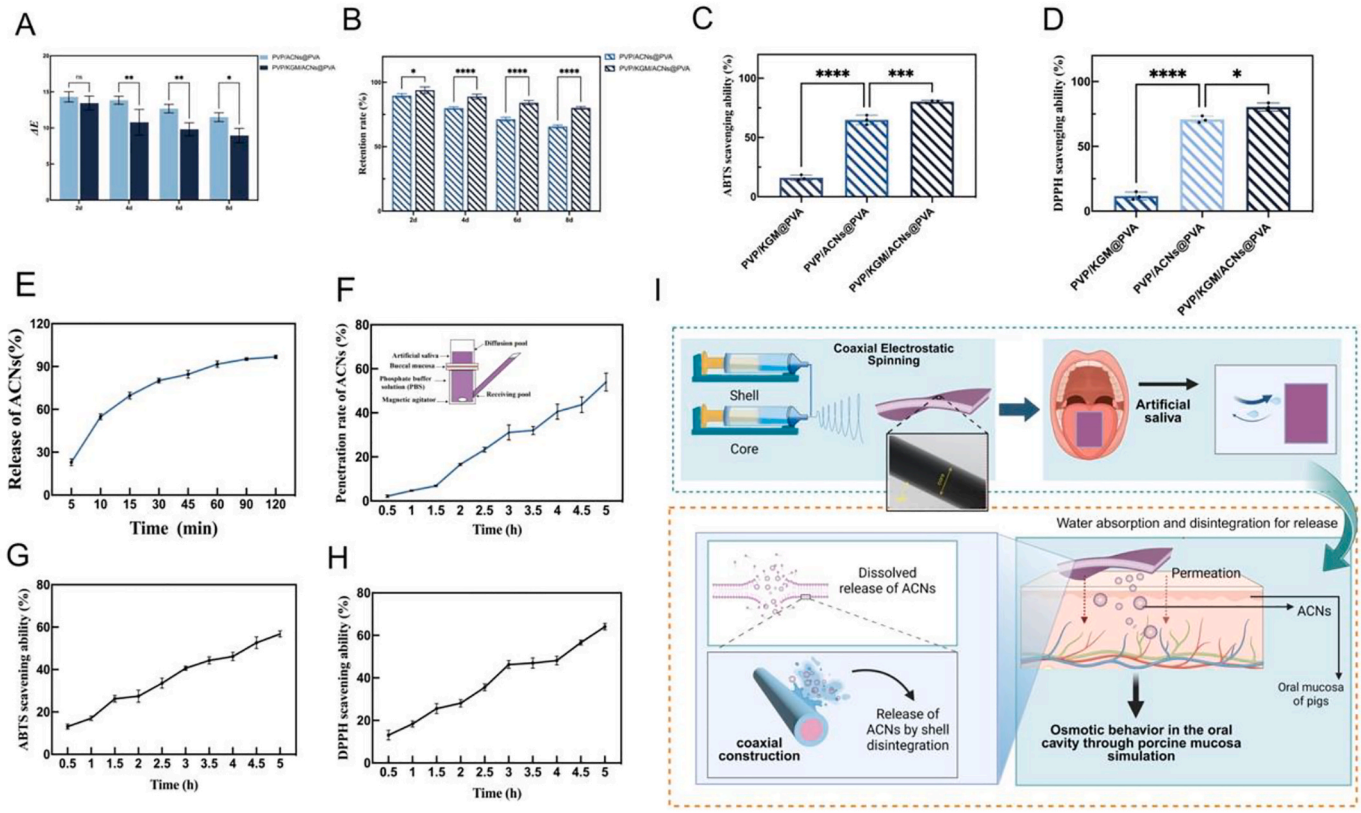

Fig. 7. (A-B) Changes in color and retention rate of PVP/ACNs@PVA and PVP/KGM/ACNs@PVA after 8 days of light exposure. (C-D) PVP/KGM@PVA, PVP/ACNs@PVA, PVP/KGM/ACNs@PVA are ABTS and DPPH scavenging ability. NFM simulation of oral release and permeation (E-I). (E) NFM released in vitro at 5, 10, 15, 30, 45, 60, 90, 120 min. (F) NFM infiltrated in vitro at 0.5, 1, 1.5, 2, 2.5, 3, 3.5, 4, 4.5, 5 h. (G, H) ABTS and DPPH scavenging ability within 5 h of NFM permeation. (I) NFM applications, Preparation and uptake process of NFM, Significance levels labeled*$P < 0.05$, **$P < 0.01$, and***$P < 0.001$, were used to represent significant differences.N.S. was used to indicate no significant difference.

diffusion of pigment molecules under light exposure (Li et al., 2024). On the other hand, it may be attributed to the unique core-shell structure constructed by the coaxial electrostatic spinning technique, in which the outer shell is tightly wrapped around the inner core. This structure significantly enhances the ability to block UV rays and effectively reduces the transmission rate of light. In summary, the shell-core structure prepared by the coaxial method showed superior performance in coping with light stress and helped to maintain the Stability of ACNs content.

3.4.2. *Evaluation of antioxidant properties*

To assess the impact of long-term light exposure on the stability of functional components in load-bearing anthocyanin oral films, this study used day 8 as a key time point to compare the decline patterns of antioxidant activity, aiming to clarify the quantitative relationship between light exposure duration and activity retention rates for PVP/ACNs@PVA and PVP/KGM/ACNs@PVA. The antioxidant activity was significantly enhanced in the loaded PVP/KGM/ACNs@PVA group when PVP/ACNs@PVA and PVP/KGM/ACNs@PVA were compared. The PVP/ACNs@PVA group only exhibited lower antioxidant properties (Fig. 7C–D). The results indicated that the constructed coaxial spinning structure synergized with the physical barrier effect of the KGM molecular chain, which effectively maintained the chemical stability of the antioxidant active ingredients during the preparation of the membrane agent.

3.4.3. *In vitro release evaluation*

The curves of cumulative release time of orally soluble membranes loaded with ACNs prepared by coaxial electrostatic spinning are shown in Fig. 7E. From the results of the release kinetics, it was concluded that the ACNs were a slowrelease process. At 5 min-30 min, which is the initial diffusion stage of the core layer, a small amount of ACNs diffused through the micropores or incompletely closed regions of the shell layer. The release rate of ACNs at this time is from 21% to 80%. At 45-120 min is the dissolution dominant stage, the shell layer gradually dissolution and the release rate is synchronized with the material degradation rate. At the end of 120 min ACNs reached 97% near complete release. It is worth noting that the hydrophilic shell layer PVA absorbs water and dissolves to achieve the diffusion rate by regulating the degree of cross-linking. Thus, the release profile of PVP/KGM/ACNs@PVA then follows a sustained release pattern. The core-shell structure NFM effectively suppresses the initial burst release of ACNs through its unique spatial confinement effect and interfacial regulation. Therefore, ACNs have a better release behavior in PVP/KGM@PVA carriers, which facilitates the application of NFM in the local oral environment.

3.4.4. *Oral absorption simulation evaluation*

In *vitro* permeation testing is performed under conditions as similar as possible to in *vitro* release, but it is a valuable study. Can be used to determine feasibility or potential advantages of oral delivery of ACNs, and the permeation process is illustrated in Fig. 7I. In this study, we evaluated the mucosal permeation kinetic characteristics of the ACNs in the coaxial electrostatically spun drug-carrying membranes in the construction of an experimental system that was highly mimicked with the physiological environment of the oral delivery of the drug. permeation kinetic characteristics. The permeation of ACNs in coaxial electrostatically spun membranes in isolated porcine mucosa was studied for 5 h. The experimental results showed that effective mucosal permeation of ACNs was achieved within the initial 0.5 h, and the amount of permeation showed a significant time-dependent increase, and the permeation rate could reach 53.96% after 5 h (Fig. 7F). This discovery not only

validates the unique structural advantages of electrospun membranes as oral sustained-release delivery systems but also provides a solid theoretical foundation for subsequent design optimization and application expansion based on this structure.

In order to investigate the antioxidant activity of ACNs in membrane agents after absorption, the present study used Franz diffusion cell to construct an *ex vivo* model of porcine oral mucosa to simulate the antioxidant activity after absorption in humans (Fig. 7G and H). The experimental results showed that the antioxidant activity in the mucosal receptor fluid showed a significant time-dependent positive correlation with the cumulative penetration of ACNs. The continuous increase in the concentration of ACNs in the mucosal layer over a 5h period also enhanced the clearance of ABTS (from initial 13.42% to 55.93%) and DPPH (from initial 14.23% to 63.97%). This study demonstrated that the ACNs still possessed antioxidant functions after simulated oral absorption.

3.5. NFM cytotoxicity analysis

As shown in Fig. S8A–C, compared with the blank control group, all experimental groups (PVP/KGM@PVA, PVP/ACNs@PVA, and PVP/KGM/ACNs@PVA) exhibited cell viability exceeding 90% after 24 h and 48 h of culture, with no statistically significant differences. Particularly in the PVP/KGM/ACNs@PVA group, cell viability remained at a high level (>92%) after 48 h, indicating that this composite membrane material did not induce significant cytotoxicity. This excellent biocompatibility can be attributed to several factors. First, the selected base materials PVP, KGM, and PVA are all recognized biocompatible polymers widely used in pharmaceutical and food applications. PVP exhibits good water solubility and low toxicity, often serving as a drug carrier. KGM, a natural polysaccharide, possesses excellent biodegradability and mucosal affinity. PVA, valued for its superior film-forming properties and biological inertness, is commonly used in medical dressings and drug delivery matrices. The loaded ACNs themselves are natural antioxidant components that are non-toxic to cells within a certain concentration range and may even exert protective effects. In summary, MTT assay results demonstrate that the prepared PVP/KGM/ACNs@PVA nanofiber membrane exhibits favorable in vitro cellular compatibility and biosafety, providing crucial toxicological evidence for its further application in oral mucosal delivery systems.

3.6. Conclusion

This study confirms that the “spatial interlocking structure” formed by the interpenetrating network of the core-shell layer can stably construct a coaxial orally disintegrating film (PVP/KGM/ACNs@PVA). The dynamic stable structure formed by hydrogen bonds between the core-shell layers endows it with excellent fiber-forming properties and physical properties. The addition of KGM enhances the stability and penetration-enhancing properties of anthocyanins, while also imparting exceptional mucosal adhesion to the base material: when simulated oral absorption and release occur, it rapidly forms a viscous gel upon contact with saliva, tightly adhering to the mucosa to prolong anthocyanin retention time and reduce loss due to rinsing and swallowing. Simultaneously, it creates a local high-concentration “reservoir,” leveraging concentration gradients to overcome low liposolubility barriers and achieve efficient trans-mucosal absorption. In addition, the synergistic regulation of the core-shell release may enhance permeability efficiency through slight disturbance of the mucous layer, ultimately significantly accelerating and improving the direct oral absorption of anthocyanins and enhancing bioavailability. This study provides a novel functional oral film agent for the effective protection and delivery of bioactive compounds.

Despite the promising results, this study has certain limitations that should be acknowledged. Firstly, the evaluation of mucosal permeation and release kinetics was conducted primarily under in vitro conditions using porcine mucosa. While this model provides valuable insights, it cannot fully replicate the dynamic and complex microenvironment of the human oral cavity, including the continuous flow of saliva, enzymatic activity, and the presence of microbial flora. Secondly, although preliminary cytotoxicity assays indicated good biocompatibility, a comprehensive assessment of long-term *in vivo* safety, potential mucosal irritation, and systemic biodistribution of the NFM and its components is warranted before clinical translation. Addressing these aspects will be crucial for advancing this delivery system from a proof-of-concept stage toward practical applications in functional foods or nutraceuticals.

Author contributions

Falin Sun: Data curation, Writing-Original draft preparation, Methodology. Guoqiang Zhang: Data curation, Methodology. Qingying Dong: Resources. Baoru Yang: Conceptualization. Ying Zhou: Conceptualization. Rodrigo Quintana Loyolad:Visualization. Yanzhe Alfonso Rene: Conceptualization. Bin Li: Conceptualization, Project administration. Jinlong Tian: Supervision; conceptualization; writing-review and editing; funding acquisition, Resources.

Declaration of competing interest

The authors declare that they have no known competing financial interests or personal relationships that could have appeared to influence the work reported in this paper.

Acknowledgment

The National Key R&D Program of China (2024YFD1600604).

Appendix A. Supplementary data

Supplementary data to this article can be found online at https://doi.org/10.1016/j.crfs.2026.101392.

References

Akcicek, A., Ozgolet, M., Tekin-Cakmak, Z.H., Karasu, S., Duran, E., Sagdic, O., 2024. Cold-pressed okra seed oil byproduct as an ingredient for muffins to decrease glycemic index, maillard reaction, and oxidation. ACS Omega 9 (7), 7491–7501. https://doi.org/10.1021/acsomega.3c06027.

Bao, Y., Wang, M., Si, X., Li, D., Gui, H., Jiang, Q., Li, J., Yang, S., Yang, Y., Li, Z., Li, B., 2024a. Customized development of 3D printed anthocyanin-phycocyanin polychromatic oral film via chondroitin sulfate homeostasis: a platform based on starch and kappa-carrageenan. Carbohydr. Polym. 330, 121817. https://doi.org/10.1016/j.carbpol.2024.121817.

Chen, Y., Wang, S., Yang, C., Zhang, L., Li, Z., Jiang, S., Bai, R., Ye, X., Ding, W., 2024. Chitosan/konjac glucomannan bilayer films: physical, structural, and thermal properties. Int. J. Biol. Macromol. 257 (Pt 2), 128660. https://doi.org/10.1016/j.ijbiomac.2023.128660.

Dharmansh, 2018. Stability analysis of an electrospinning jet of newtonian and polymeric fluids. Polymer.

Dodero, A., Williams, R., Gagliardi, S., Vicini, S., Alloisio, M., Castellano, M., 2019. A micro-rheological and rheological study of biopolymers solutions: hyaluronic acid. Carbohydr. Polym. 203, 349–355. https://doi.org/10.1016/j.carbpol.2018.09.072.

Kali, G., Ozkahraman, B., Laffleur, F., Knoll, P., Wibel, R., Zoller, K., Bernkop-Schnurch, A., 2023. Thiolated cellulose: a dual-acting mucoadhesive and permeation-enhancing polymer. Biomacromolecules 24 (11), 4880–4889. https://doi.org/10.1021/acs.biomac.3c00577.

Kazemianrad, F., Koocheki, A., Ghorani, B., 2023. Encapsulation of caffeine in sandwich structured alyssum homolocarpum seed gum/PVA/gelatin nanofibers using electrospinning technique. Food Hydrocoll. 140. https://doi.org/10.1016/j.foodhyd.2023.108604.

Kurakula, M., Koteswara Rao, G.S.N., 2020. Moving polyvinyl pyrrolidone electrospun nanofibers and bioprinted scaffolds toward multidisciplinary biomedical applications. Eur. Polym. J. 136. https://doi.org/10.1016/j.eurpolymj.2020.109919.

Lan, Y.-C., Lai, L.-S., 2023. Pasting and rheological properties of water caltrop starch as affected by the addition of konjac glucomannan, guar gum and xanthan gum. Food Hydrocoll. 136. https://doi.org/10.1016/j.foodhyd.2022.108245.

Li, B., Bao, Y., Li, J., Bi, J., Chen, Q., Cui, H., Wang, Y., Tian, J., Shu, C., Wang, Y., Lang, Y., Zhang, W., Tan, H., Huang, Q., Si, X., 2022. A sub-freshness monitoring chitosan/starch-based colorimetric film for improving color recognition accuracy via

controlling the pH value of the film-forming solution. Food Chem. 388, 132975. https://doi.org/10.1016/j.foodchem.2022.132975.

Li, J., Bao, Y., Li, Z., Cui, H., Jiang, Q., Hou, C., Wang, Y., Wu, Y., Shang, J., Xiao, Y., Shu, C., Wang, Y., Wen, B., Si, X., Li, B., 2023. Dual-function beta-cyclodextrin/starch-based intelligent film with reversible responsiveness and sustained bacteriostat-releasing for food preservation and monitoring. Int. J. Biol. Macromol. 253 (Pt 5), 127168. https://doi.org/10.1016/j.ijbiomac.2023.127168.

Li, X., Xiao, N., Xiao, G., Bai, W., Zhang, X., Zhao, W., 2021. Lemon essential oil/vermiculite encapsulated in electrospun konjac glucomannan-grafted-poly (acrylic acid)/polyvinyl alcohol bacteriostatic pad: sustained control release and its application in food preservation. Food Chem. 348, 129021. https://doi.org/10.1016/j.foodchem.2021.129021.

Li, Y., Li, K., Guo, Y., Liu, Y., Zhao, G., Qiao, D., Jiang, F., Zhang, B., 2024. Mechanism for the synergistic gelation of konjac glucomannan and kappa-carrageenan. Int. J. Biol. Macromol. 277 (Pt 3), 134423. https://doi.org/10.1016/j.ijbiomac.2024.134423.

Liu, X., Sun, Y., Wang, J., Kang, Y., Wang, Z., Cao, W., Ye, J., Gao, C., 2024. A tough, antibacterial and antioxidant hydrogel dressing accelerates wound healing and suppresses hypertrophic scar formation in infected wounds. Bioact. Mater. 34, 269–281. https://doi.org/10.1016/j.bioactmat.2023.12.019.

Lu, Y., Jin, G., Xiao, P., Jinshan, Q., Chao, T., 2021. Cellulose insulation paper with high thermal stability and low polarizability: influence of different substituents on POSS modified cellulose insulating paper. Cellulose 28 (10), 6023–6033. https://doi.org/10.1007/s10570-021-03956-x.

Ma, T., Chen, J., 2025. Multiple dimensional rheology approach for oral texture prediction of yogurts. Food Hydrocoll. 160. https://doi.org/10.1016/j.foodhyd.2024.110745.

Pandey, M., Choudhury, H., Ying, J.N.S., Ling, J.F.S., Ting, J., Ting, J.S.S., Zhia Hwen, I. K., Suen, H.W., Samsul Kamar, H.S., Gorain, B., Jain, N., Mohd Amin, M.C.I., 2022. Mucoadhesive nanocarriers as a promising strategy to enhance intracellular delivery against oral cavity carcinoma. Pharmaceutics 14 (4). https://doi.org/10.3390/pharmaceutics14040795.

Ran, X., Yang, H., 2022. Promoted strain-hardening and crystallinity of a soy protein-konjac glucomannan complex gel by konjac glucomannan. Food Hydrocoll. 133. https://doi.org/10.1016/j.foodhyd.2022.107959.

Serrano, D.R., Fernandez-Garcia, R., Mele, M., Healy, A.M., Lalatsa, A., 2019. Designing fast-dissolving orodispersible films of amphotericin B for oropharyngeal candidiasis. Pharmaceutics 11 (8). https://doi.org/10.3390/pharmaceutics11080369.

Sha, H., Yuan, C., Cui, B., Zhao, M., Wang, J., 2022. Pre-gelatinized cassava starch orally disintegrating films: influence of β-Cyclodextrin. Food Hydrocoll. 123. https://doi.org/10.1016/j.foodhyd.2021.107196.

Song, B., Li, H., Tian, J., Zhang, Y., Li, Z., Wang, J., Wang, Y., Si, X., Li, B., 2023. Mechanism of sugar degradation product 5-hydroxymethylfurfural reducing the stability of anthocyanins. Food Chem. 419, 136067. https://doi.org/10.1016/j.foodchem.2023.136067.

Su, W., Chang, Z., E, Y., Feng, Y., Yao, X., Wang, M., Ju, Y., Wang, K., Jiang, J., Li, P., Lei, F., 2024. Electrospinning and electrospun polysaccharide-based nanofiber membranes: a review. Int. J. Biol. Macromol. 263 (Pt 2), 130335. https://doi.org/10.1016/j.ijbiomac.2024.130335.

Sun, F.-L., Zhao, M.-Y., Li, Y., Li, Z.-Y., Li, X.-J., Wang, N., Hu, B.-W., Xue, H.-Y., Zhao, M., Tian, J.-L., 2025. Research progress of electrospinning in food field: a review. Food Hydrocoll. 158. https://doi.org/10.1016/j.foodhyd.2024.110474.

Tan, C., Celli, G.B., Abbaspourrad, A., 2018. Copigment-polyelectrolyte complexes (PECs) composite systems for anthocyanin stabilization. Food Hydrocoll. 81, 371–379. https://doi.org/10.1016/j.foodhyd.2018.03.011.

Tan, P., Wang, H., Xiao, F., Lu, X., Shang, W., Deng, X., Song, H., Xu, Z., Cao, J., Gan, T., Wang, B., Zhou, X., 2022. Solution-processable, soft, self-adhesive, and conductive polymer composites for soft electronics. Nat. Commun. 13 (1), 358. https://doi.org/10.1038/s41467-022-28027-y.

Tang, S., Si, X., Zang, Z., Gui, H., Xie, X., Wang, L., He, Y., Yang, B., Li, B., 2024. Mildly preheating induced conformational changes of soy protein isolates contributed to the binding interaction with blueberry anthocyanins for stabilization. Food Hydrocoll. 155. https://doi.org/10.1016/j.foodhyd.2024.110209.

Terlau, F., Martin, H.M., Galstyan, A., 2024. Visualizing active sites in electrospun photoactive membranes via fluorescence lifetime imaging. Angew. Chem. Int. Ed. 63 (50), e202414412. https://doi.org/10.1002/anie.202414412.

Wang, H., Fan, T., Zeng, Z., Chen, Z., Lu, M., Zhou, M., Qin, X., Liu, X., 2024. Use of ozone oxidation in combination with deacetylation for improving the structure and gelation properties of konjac glucomannan. Food Chem. 453, 139599. https://doi.org/10.1016/j.foodchem.2024.139599.

Wang, J., Shan, H., Qin, Y., Qin, D., Zhao, W., Yang, Z., Kong, L., Li, S., 2025. Electrospinning zein with theaflavin: production, characterization, and application in active packaging for cold-fresh pork. Int. J. Biol. Macromol. 287, 138594. https://doi.org/10.1016/j.ijbiomac.2024.138594.

Wang, L.X., Dao, L.P., Guo, Q.Y., Chen, T.L., Fu, L.J., Zhou, F.C., Yuan, Y., 2022. Investigation on the influence of AC electric filed and KCl on the structure and gel properties of Konjac glucomannan. Food Chem. 386, 132755. https://doi.org/10.1016/j.foodchem.2022.132755.

Wen, P., Hu, T.G., Li, L., Zong, M.H., Wu, H., 2018. A colon-specific delivery system for quercetin with enhanced cancer prevention based on co-axial electrospinning. Food Funct. 9 (11), 5999–6009. https://doi.org/10.1039/c8fo01216d.

Wu, G., Yin, Y., Li, C., Hao, R., Zang, J., Kang, M., Luo, D., Xu, W., 2024. Sustained release behavior of lysozyme based on konjac glucomannan/κ-carrageenan composite hydrogels. Lwt 201. https://doi.org/10.1016/j.lwt.2024.116274.

Xu, C., Ma, J., Liu, Z., Wang, W., Liu, X., Qian, S., Chen, L., Gu, L., Sun, C., Hou, J., Jiang, Z., 2023. Preparation of shell-core fiber-encapsulated Lactobacillus rhamnosus 1.0320 using coaxial electrospinning. Food Chem. 402, 134253. https://doi.org/10.1016/j.foodchem.2022.134253.

Yuan, Y., Tian, H., Huang, R., Liu, H., Wu, H., Guo, G., Xiao, J., 2023. Fabrication and characterization of natural polyphenol and ZnO nanoparticles loaded protein-based biopolymer multifunction electrospun nanofiber films, and application in fruit preservation. Food Chem. 418. https://doi.org/10.1016/j.foodchem.2023.135851.

Zhang, H., Ji, Y., Yuan, C., Sun, P., Xu, Q., Lin, D., Han, Z., Xu, X., Zhou, Q., Deng, J., 2022. Fabrication of astaxanthin-loaded electrospun nanofiber-based mucoadhesive patches with water-insoluble backing for the treatment of oral premalignant lesions. Mater. Des. 223. https://doi.org/10.1016/j.matdes.2022.111131.

Zhang, W., Li, X., Ma, X., Li, H., Liu, J., Zeng, Y., Cai, D., Xu, Q., Chen, G., Tian, L., Sun, J., Bai, W., 2024. Microencapsulation of anthocyanins extracted from black soybean peels by whey protein/fructo-oligosaccharide contributes to improved stability, bioavailability, and ability to regulate glycolipid metabolism. Food Frontiers 5 (2), 570–583. https://doi.org/10.1002/fft2.333.

Zhao, J., Chen, L., Ma, A., Bai, X., Zeng, Y., Liu, D., Liu, B., Zhang, W., Tang, S., 2024. Recent advances in coaxial electrospun nanofibers for wound healing. Mater. Today Bio 29, 101309. https://doi.org/10.1016/j.mtbio.2024.101309.